Magnetism, X-rays and accretion rates in WD 1145+017 and other polluted white dwarf systems

J. Farihi,[1]⋆† L. Fossati,[2] P. J. Wheatley,[3] B. D. Metzger,[4] J. Mauerhan,[5]
S. Bachman,[6,7] B. T. Gänsicke,[3] S. Redfield,[7] P. W. Cauley,[7] O. Kochukhov,[8]
N. Achilleos[1] and N. Stone[9]

[1]*Department of Physics and Astronomy, University College London, London WC1E 6BT, UK*
[2]*Space Research Institute, Austrian Academy of Sciences, A-8042 Graz, Austria*
[3]*Department of Physics, University of Warwick, Coventry CV4 7AL, UK*
[4]*Department of Physics, Columbia University, New York 10027, USA*
[5]*Department of Astronomy, University of California, Berkeley 94270, USA*
[6]*Department of Physics, Indiana University of Pennsylvania, Indiana 15705, USA*
[7]*Astronomy Department and Van Vleck Observatory, Wesleyan University, Middletown 06459, USA*
[8]*Department of Physics and Astronomy, Uppsala University, E-752 36 Uppsala, Sweden*
[9]*Department of Astronomy, Columbia University, New York 10027, USA*

ABSTRACT

This paper reports circular spectropolarimetry and X-ray observations of several polluted white dwarfs including WD 1145+017, with the aim to constrain the behaviour of disc material and instantaneous accretion rates in these evolved planetary systems. Two stars with previously observed Zeeman splitting, WD 0322−019 and WD 2105−820, are detected above 5σ and $\langle B_z \rangle > 1\,$kG, while WD 1145+017, WD 1929+011, and WD 2326+049 yield (null) detections below this minimum level of confidence. For these latter three stars, high-resolution spectra and atmospheric modelling are used to obtain limits on magnetic field strengths via the absence of Zeeman splitting, finding $B_* < 20\,$kG based on data with resolving power $R \approx 40\,000$. An analytical framework is presented for bulk Earth composition material falling on to the magnetic polar regions of white dwarfs, where X-rays and cyclotron radiation may contribute to accretion luminosity. This analysis is applied to X-ray data for WD 1145+017, WD 1729+371, and WD 2326+049, and the upper bound count rates are modelled with spectra for a range of plasma $kT = 1$–$10\,$keV in both the magnetic and non-magnetic accretion regimes. The results for all three stars are consistent with a typical dusty white dwarf in a steady state at 10^8–$10^9\,$g s^{-1}. In particular, the non-magnetic limits for WD 1145+017 are found to be well below previous estimates of up to $10^{12}\,$g s^{-1}, and likely below $10^{10}\,$g s^{-1}, thus suggesting the star-disc system may be average in its evolutionary state, and only special in viewing geometry.

Key words: circumstellar matter – stars: magnetic field – planetary systems – white dwarfs – X-rays: stars.

1 INTRODUCTION

It is now abundantly clear that a significant fraction of planetary systems survive the gauntlet of stellar evolution and manifest around white dwarf stars (Farihi 2016; Veras 2016). These evolved planetary systems provide empirical and theoretical constraints on planet formation and evolution that are complimentary to conventional

studies, and most importantly provide information unavailable via pre-main and main-sequence stars. Protoplanetary discs reveal ongoing chemical and spatial processes related to the earliest stages of planet formation, and especially volatile grain chemistry and dust trapping (Pontoppidan et al. 2014; van der Marel et al. 2016) prior to and possibly during their incorporation into large bodies. Young and mature main-sequence stars reveal systems of fully fledged planets, their planetesimal belt leftovers, and (giant impact) collisional by-products (Meng et al. 2014; Chauvin et al. 2017; MacGregor et al. 2017). These planetary systems yield final architectures and assemblies, where the physical and chemical processes

⋆ E-mail: j.farihi@ucl.ac.uk
† STFC Ernest Rutherford Fellow.

associated with planet formation are essentially exhausted and thus must be inferred via modelling. White dwarfs are the only systems to provide bulk chemical information on large planetesimals and an alternative window on to planetary systems born around A- and F-type stars.

More than a decade of observational evidence supports a picture where minor or major planets experience catastrophic fragmentation within the Roche limit of white dwarfs (Jura 2003). This paradigm is supported by multiple lines of evidence including atmospheric pollution via heavy elements (Zuckerman et al. 2003; Farihi et al. 2010; Koester, Gänsicke & Farihi 2014), infrared and optical emission from closely orbiting discs of dust and gas (Farihi 2016), and chemical abundances broadly consistent with terrestrial-like planetesimals (Gänsicke et al. 2012; Jura & Young 2014; Wilson et al. 2016). Evidence for short-term disc evolution has been observed in gas and dust emission features, including evidence of eccentric disc precession (Wilson et al. 2014; Xu & Jura 2014; Manser et al. 2016). Arguably the most spectacular example of ongoing change in a white dwarf debris disc is the rapidly varying (over minutes to months) extinction observed in both photometry and spectroscopy towards WD 1145+017 (Vanderburg et al. 2015; Gänsicke et al. 2016; Rappaport et al. 2016; Redfield et al. 2017).

Theoretical progress on evolved planetary system dynamics, dust production, and disc evolution has been invaluable for placing the observations in context. The lifetime of dust grains in flat discs that are (vertically) optically thick, will be driven by Poynting–Robertson drag (Rafikov 2011), as this configuration can effectively damp grain–grain collisions that would otherwise be more than an order of magnitude more rapid (Farihi, Zuckerman & Becklin 2008). The presence of gas within discs may influence their evolution by dust–gas coupling (Metzger, Rafikov & Bochkarev 2012) or α-disc viscous dissipation (Jura 2008), and this may result in shorter disc lifetimes than by dust evolution alone (Bochkarev & Rafikov 2011). There is indirect evidence for historical changes in accretion rate over pollution lifetime seen in samples of stars with disparate metal sinking time-scales (Girven et al. 2012), and this appears to arise from relatively short-lived episodes of dust and gas production (Farihi et al. 2012; Wyatt et al. 2014). Recent work suggests that collisional cascades can dominate disc behaviour at orbital radii comparable to the Roche limit, resulting in discs with significant vertical scale heights and substantially shorter lifetimes in the absence of replenishment (Kenyon & Bromley 2017).

The prevalent model for WD 1145+017 involves at least one parent body orbiting near the Roche limit and losing mass in a tail-like and possibly a head-like feature, potentially in discrete events that are eventually transformed into large clouds of gas and debris (Vanderburg et al. 2015; Rappaport et al. 2016). In this scenario, the parent body or bodies are comparable in mass to the largest solar system asteroids, and this in turn places strong constraints on orbital and structural stability, implying essentially circular orbits and a relatively brief time period until total disintegration (Veras, Marsh & Gänsicke 2016; Gurri, Veras & Gänsicke 2017; Veras et al. 2016). Outstanding issues include the apparently circular orbit of one or more large planetary bodies at the Roche limit, and the likelihood of witnessing a short-lived event at a narrow range of possible viewing angles. Recently, a novel model proposed that dust trapping in the stellar magnetosphere could, under favourable circumstances, be consistent with the quasi-periodic extinction seen towards WD 1145+017 (Farihi, von Hippel & Pringle 2017b).

Previous observation-based analyses suggested that WD 1145+017 may be currently accreting at a rate significantly higher than inferred to be ongoing for any polluted white dwarf, and up to $10^{12}\,\mathrm{g\,s^{-1}}$ (Gänsicke et al. 2016; Rappaport et al. 2016; Xu et al. 2016). This rate is $\sim 10^2$ times higher than the steady-state inference from the heavy elements in the stellar atmosphere, and $\sim 10^3$ times higher than any instantaneous rate inferred via a steady-state regime calculation.

This paper presents X-ray observations to confirm or rule out the previously proposed high accretion rate for WD 1145+017, and corresponding circular spectropolarimetry to determine if either circumstellar dust, or the process of accretion is influenced by stellar magnetism. The observational data are presented in Section 2 with the resulting upper limits and physical constraints derived in Section 3. This analysis includes a set of models that link magnetic field strength and accretion rate with the emergent luminosity of the cooling flow and corresponding physical mechanisms, including X-ray emission. Section 3 also includes a new high-resolution spectrum of WD 1145+017 that indicates the observed circumstellar gas is not in the process of accreting. Section 4 provides a summary of constraints for the accretion rates onto WD 1145+017 and other polluted white dwarfs, as well as conclusions.

The remainder of the paper refers to stars by their numerical designation alone.

2 OBSERVATIONS AND DATA

As magnetic fields will influence the flow and luminosity of the accretion, the observational data appear in the following natural order.

2.1 Optical spectropolarimetry

Five metal-rich white dwarfs – including 1145+017 – were observed as part of an ongoing search for weak stellar magnetism in evolved planetary systems where accretion from circumstellar matter is evident. Each star was observed in spectropolarimetric mode with the Focal Reducer and low dispersion Spectrograph (FORS2; Appenzeller et al. 1998), which is mounted on UT1 of the ESO Very Large Telescope (VLT). The targets were observed using either the 1200R grating and a 1″.0 slit, or with the 1200B grating and a 0″.7 slit, and all exposures were performed alternating the position of the quarter-wave retarder plate at $\pm 45°$. All data were taken in service mode with the MIT red-sensitive detector (the E2V blue-sensitive chip is only available in visitor mode), and read out using 2×2 binning. Table 1 lists the target properties and observing details.

Three $T_{\mathrm{eff}} > 10\,000\,\mathrm{K}$ DAZ stars were observed over the H α region as this line is the strongest in their optical spectra, and their weak metal lines are not readily detectable at the modest resolution of FORS2: 1929+011 ($= $ GALEX J193156.8+011745), 2105–820 ($= $ LTT 8381), and 2326+049 ($= $ G29-38). These three stars were chosen in P97 to be relatively nearby and bright examples of polluted white dwarfs, and thus where the strongest constraints could be placed on stellar magnetism. In P98, 0322–019 ($= $ G77-50) and 1145+017 were observed as control and science targets, respectively, where their distinct optical spectra required coverage at blue wavelengths. For both stars the Ca II H and K lines are the deepest spectral features, with weak or undetectable H lines at modest resolution (Farihi et al. 2011; Xu et al. 2016).

The data were reduced and analysed using a set of IRAF and IDL routines described in detail by Fossati et al. (2015), developed based on previously published techniques and algorithms for spectropolarimetry (Bagnulo et al. 2012, 2013). Because of cosmic rays affecting the data obtained in P98, the spectra were retrieved via weighted (optimal) extraction.

Table 1. FORS2 spectropolarimetry and longitudinal magnetic field measurements.

WD#	V (mag)	SpT[a]	T_{eff} (K)	Date	Grating	Coverage (Å)	t_{exp} (s)	S/N	$\langle B_z \rangle$[b] (kG)	$\langle N_z \rangle$ (kG)
0322–019	16.1	DZA	5300	2016 Oct 04	1200B+97	3660–5110	4×310	70	$-5.4 \pm 3.0\ (1.8\sigma)$	$+4.3 \pm 2.6\ (1.6\sigma)$
				2016 Oct 05	1200B+97	3660–5110	4×310	90	$\mathbf{-16.5 \pm 2.3\ (7.1\sigma)}$	$-1.7 \pm 2.1\ (0.8\sigma)$
1145+017	17.2	DBZA	15 900	2017 Jan 01	1200B+97	3660–5110	8×594	130	$-0.1 \pm 0.4\ (0.2\sigma)$	$-0.7 \pm 0.4\ (1.7\sigma)$
				2017 Jan 02	1200B+97	3660–5110	4×594	110	$-1.0 \pm 0.4\ (2.4\sigma)$	$-0.2 \pm 0.4\ (0.4\sigma)$
				2017 Feb 01	1200B+97	3660–5110	4×594	120	$\mathbf{+1.0 \pm 0.3\ (3.5\sigma)}$	$-0.1 \pm 0.3\ (0.5\sigma)$
				2017 Feb 27	1200B+97	3660–5110	4×594	110	$-0.6 \pm 0.4\ (1.5\sigma)$	$+0.5 \pm 0.4\ (1.2\sigma)$
1929+011	14.2	DAZ	21 200	2016 Aug 04	1200R+93	5750–7310	4×500	320	$+0.5 \pm 0.4\ (1.2\sigma)$	$+0.1 \pm 0.4\ (0.3\sigma)$
2105–820	13.8	DAZ	10 200	2016 June 30	1200R+93	5750–7310	4×300	350	$\mathbf{+5.1 \pm 0.3\ (15.2\sigma)}$	$-0.2 \pm 0.3\ (0.6\sigma)$
2326+049	13.0	DAZ	11 900	2016 Aug 04	1200R+93	5750–7310	4×120	290	$-0.7 \pm 0.5\ (1.4\sigma)$	$+0.1 \pm 0.5\ (0.2\sigma)$

Notes. [a]White dwarf spectral types begin with 'D' for degenerate star, followed by letters corresponding to elements in decreasing line strengths: e.g. 'A' for Balmer absorption, 'B' for He I lines, and 'Z' for metal features (McCook & Sion 1999).
[b]P98 measurements are for metal and He I lines, while P97 determinations are based on Hα (see Section 2.1).

The surface-averaged, longitudinal magnetic field $\langle B_z \rangle$ was measured using the following formula (Angel & Landstreet 1970; Landstreet et al. 1975) and least-squares fitting (Bagnulo et al. 2002, 2012):

$$V_\lambda = -g_{eff}\, C_z\, \lambda^2 \frac{1}{I_\lambda} \frac{dI_\lambda}{d\lambda} \langle B_z \rangle, \qquad (1)$$

where V_λ and I_λ are the Stokes V and I profiles, respectively. The effective Landé factor, g_{eff}, was set to be 1.25 except in the region of the Balmer lines where it was set to 1.0. The constant in the equation is defined as $C_z = e/4\pi m_e c^2 \approx 4.7 \times 10^{-13}$ Å^{-1} G^{-1}, where e is the electron charge, m_e the electron mass, and c the speed of light.

In addition to $\langle B_z \rangle$, $\langle N_z \rangle$ was also measured and denotes the value of the surface-averaged, longitudinal magnetic field obtained from the diagnostic N profile (Donati et al. 1997) in place of Stokes V. The N profile is in practice the difference between an even number of Stokes V profiles and as such provides a measure of the noise in the spectra, and $\langle N_z \rangle$ can highlight possible spurious detections. In addition, the N profile permits statistical checks for an improved assessment of any genuine magnetic fields (Bagnulo et al. 2013; Fossati et al. 2015). The Stokes V and N parameter spectra of 1145+017 showed rather large-scale deviations from zero, and these spectra were therefore renormalized using high-order polynomials.

The $\langle B_z \rangle$ and $\langle N_z \rangle$ values were derived considering spectral windows covering either only hydrogen lines, or only metallic lines (including He I). Owing to the wavelength coverage, modest spectral resolution, and intrinsic weakness of their metal features, spectropolarimetry was performed only on the strong Hα features of the P97 targets 1929+011, 2105–820, and 2326+049. In contrast, the P98 targets 0322–019 and 1145+017 have hydrogen lines that are relatively weak compared to their other absorption features, and hence spectropolarimetry for these stars was carried out on metal and He I lines. A careful selection of lines was done for 1145+017 based on a HIRES spectrum with resolving power $R \approx 40\,000$ as a reference. Results are listed in Table 1 and plotted in Fig. 1.

Magnetic field measurements conducted with low-resolution spectropolarimeters mounted at Cassegrain focus, such as FORS2, may be affected by strong systematics that may be difficult to characterize (see Bagnulo et al. 2012, 2013). In some cases, such systematics can lead to spurious $3\sigma - 4\sigma$ detections, and for this reason a magnetic field is only considered detected when above the 5σ level and with a $\langle N_z \rangle$ value consistent with zero. However, for targets in which the measured $\langle B_z \rangle$ value lies in the range 3σ–5σ, and which also exhibit $\langle N_z \rangle$ values consistent with zero, the general recommendation is to follow up with additional observations

to assess the genuine presence of a structured, large-scale magnetic field.

2.2 X-rays

1145+017 was observed as a ToO with the *X-ray Multi-Mirror Mission (XMM–Newton)* beginning 2016 June 6 for a continuous duration of 134.9 ks (observation #0790181301). Two additional polluted white dwarfs have previously been observed at X-ray wavelengths, both with *XMM*: 1729+371 (= GD 362) and 2326+049 (Jura, Farihi & Zuckerman 2009), and their data were retrieved from the archive and re-analysed here in a novel manner, as the detectability of X-rays from polluted white dwarfs in general is a focus of the present study.

Using the pipeline processed events list for 1145+017, there is no convincing evidence of a detection in either the pn or MOS detectors. The source position was corrected for the $\mu < 0\farcs 05$ yr^{-1} proper motion of the target, and counts were extracted from a 15 arcsec radius region centred at $11^h 48^m 33.58^s +01° 28' 59.3''$. The astrometric solution was also tested by inspecting other sources, and was found reliable to at least a few arcseconds. Light curves were constructed to search for a possible detection in any short time interval, but none were apparent. Data were filtered for background flares caused by solar soft protons, when the 10–12 keV count rate from the whole camera was above 0.5 counts s^{-1} for the pn, and above 0.2 and 0.3 counts s^{-1} for the MOS1 and MOS2 detectors, respectively. This reduced the weighted on-source live time to 104.7 ks for the pn detector, and 126.0 ks for the MOS detectors (including the vignetting correction).

The standard data reduction methods were followed, as described in data analysis threads provided with the Science Analysis System (SAS version 16.0). A spectrum was extracted from the source position, and an adjacent 67 arcsec radius region free of sources was used to estimate the background. Extractions were done for the energy ranges 0.3–2.0 and 0.3–10 keV on the pn and MOS detectors, as well as the full range of the pn detector 0.16–12.0 keV. Pipeline event files were used throughout, but the data were independently reprocessed and no significant differences were found for events with pattern ≤ 12 for the MOS and pattern ≤ 4 for the pn detector (which are the standard filtering choices). The data were checked with pattern $= 0$ (single pixel) events in case this reduced the background more than the sensitivity, but this did not improve the count rate limits.

Archival data for 1729+371 (20.4 ks) and 2326+049 (22.5 ks) were retrieved and similarly analysed. For all three targets, the

Table 2. *XMM* data and XSPEC model X-ray flux limits.

Energy range (keV)	Source region (counts)	Bkgd region (counts)	Upper[a] bound	Upper[a] rate (counts s^{-1})	F_{lim} ($kT = 1$ keV) In-band	Total	F_{lim} ($kT = 4$ keV) In-band	Total	F_{lim} ($kT = 10$ keV) In-band	Total
					(10^{-15} erg cm^{-2} s^{-1})					
1145+017 (126.0 ks)					**Solar composition**					
0.3–2.0	64	64	15	1.2×10^{-4}	0.4	0.7	0.5	1.2	0.5	2.1
0.3–10.0	126	134	17	1.3×10^{-4}	0.5	0.7	0.9	1.1	1.1	1.6
					Bulk Earth composition					
					0.4	0.6	0.4	1.4	0.4	3.7
					0.5	0.6	1.0	1.2	1.7	2.4
1729+371 (20.4 ks)					**Solar composition**					
0.3–2.0	7	10	5	2.3×10^{-4}	0.9	1.3	0.9	2.4	0.9	4.0
0.3–10.0	16	19	7	3.2×10^{-4}	1.3	1.7	2.1	2.5	2.6	3.8
					Bulk Earth composition					
					0.8	1.1	0.8	2.7	0.8	7.2
					1.2	1.5	2.5	2.9	4.2	5.8
2326+049 (22.5 ks)					**Solar composition**					
0.3–2.0	16	6	18	8.0×10^{-4}	3.6	5.4	3.9	10	3.9	17
0.3–10.0	25	11	23	1.0×10^{-3}	4.8	6.6	8.0	9.7	10	14
					Bulk Earth composition					
					3.4	4.7	3.3	11	3.6	30
					4.4	5.9	9.4	11	16	22

Notes. [a]These are 90 per cent confidence bounds, calculated following Kraft et al. (1991), for the combined MOS1 and MOS2 detectors.
The in-band flux calculations include absorption along the line of sight due to interstellar hydrogen, while the bolometric (total) fluxes do not.

background counts on the MOS detectors were found to be modestly to significantly lower than for the pn detector, thus yielding tighter constraints on source counts. For this reason, the derived count rate constraints were taken from the combined MOS1 and MOS2 detector results for all sources. Statistical confidence bounds on the number of source counts in each energy range were calculated following Kraft, Burrows & Nousek (1991), which is a Bayesian approach designed for low counts that adopts the prior that source counts cannot be negative. These 90 per cent confidence bounds on the source counts are not upper limits, strictly speaking, and are listed in Table 2. It is noteworthy that the upper bound MOS counts derived here for 2326+049 are approximately a factor of 3 higher than those previously published by Jura et al. (2009), and almost certainly due to contamination from a point source 15 arcsec distant. Jura et al. (2009) provide no details of corrective measures taken to remove or model the nearby source contamination, and the counts and rates listed here for 2326+049 are unmodified.

The X-ray spectral fitting package XSPEC 12.9 was used to calculate fluxes corresponding to the upper confidence bounds for given source spectra. XSPEC automatically accounts for the *XMM* instrument response and aperture correction at the target position, and allows for flexibility in model definition. The range of adopted models assumed optically thin plasmas, interstellar absorption from both grains and neutral hydrogen (Wilms, Allen & McCray 2000), with input abundances of solar (Asplund et al. 2009), chondritic (Lodders 2003), and bulk Earth (McDonough 2000) compositions. The results using the chondritic and bulk Earth compositions were found to be similar, and the former was discarded from the analysis.

Interstellar absorption for 1145+017 was assumed to have $N_{\text{H}} = 10^{20}$ cm^{-2}, which is consistent with the observed hydrogen

column density to WD 1034+001 (Oliveira et al. 2006), a star in the same direction at a comparable distance. This adopted value is also consistent with the survey of hydrogen column densities by Linsky et al. (2006), where practically all objects within 100 pc of the Sun have $N_{\text{H}} \leq 10^{19}$ cm^{-2}, and all objects within 200 pc have $N_{\text{H}} \leq 10^{20}$ cm^{-2}. The hydrogen column density towards 1729+371 and 2326+049 can be estimated in a similar way: for the former, using ι Oph from Vallerga et al. (1993), a value of $N_{\text{H}} \approx 6 \times 10^{18}$ cm^{-2} is estimated; for the latter, Kilic & Redfield (2007) estimated $N_{\text{H}} \approx 2 \times 10^{18}$ cm^{-2}. It is noteworthy that column densities differing by a factor of 2 lead to only a few per cent difference in the calculated limiting fluxes, and that the accretion column itself is not a significant source of self-absorption.

The fluxes of the model plasmas were calculated for emission temperatures of 1, 4, and 10 keV. These span the range of characteristic single temperatures seen in disc-accreting cataclysmic variables (see Baskill, Wheatley & Osborne 2005). Polars (magnetic cataclysmic variables) with column accretion can have higher characteristic temperatures, but low-state magnetic systems tend to have temperatures at the lower end (Mukai 2017). The characteristic temperature seen in X-rays will be lower than the shock temperature, and the true spectrum will be something like a cooling flow, with emission from a range of temperatures. The X-ray emission spectra are shown in Fig. 2 and plot both solar and bulk Earth composition models for the full temperature range. The models were then scaled to match the *XMM* upper bound count rates for each source, yielding upper limit detector and bolometric fluxes for each model listed in Table 2. While there is a visible difference between the spectra of solar and bulk Earth composition plasmas, the resulting flux limit, differences are less than 20 per cent in the $kT = 1$ and 4 keV cases, and within a factor of two for 10 keV.

2.3 *XMM* Optical Monitoring Data

Data from the Optical Monitor (OM) telescope was also collected for 1145+017. Observations were taken in photon-counting (FAST) mode with the *UVW1* filter, at an effective wavelength of 2910 Å. Unfortunately, there was a telescope fault after the first 35 ks and data were only recorded for the first one-fourth of the total X-ray exposure. Despite this, the OM data are plotted in Fig. 3 and show that the source was experiencing dimming events during this time. The raw data were sampled at 10 s cadence but had to be binned to 300 s intervals for features to emerge, but demonstrate there were flux drops by at least 20 per cent and likely reveal two repeating structures.

3 RESULTS AND CONTEXT

3.1 Constraints on weak magnetism

The observational incidence of magnetism among white dwarfs is well represented in the literature, but is fraught with detection and selection biases so that a coherent picture spanning cooling age and atmospheric composition has not yet emerged (Schmidt & Smith 1995; Schmidt et al. 2003; Kawka et al. 2007; Hollands, Gänsicke & Koester 2015). While the origin and manifestation of magnetic fields in degenerates is beyond the scope of this paper, the subset of relatively weak, kG-order fields at polluted white dwarfs has implications for circumstellar disc structure and accretion onto the surface (Metzger et al. 2012). Field strengths as small as 0.1–1 kG can truncate a disc at the Alfvén radius or prevent its formation as in polars, and will result in accretion near free-fall velocities onto magnetic polar regions, as opposed to equatorial accretion in a boundary layer at lower, sub-Keplerian velocities.

There are now a significant number of metal-enriched white dwarfs that exhibit (weak) magnetic fields, and this is potentially a detection bias, as Zeeman splitting can be more readily detected in narrow features from multiple species of heavy elements, than in stars with only weak Balmer lines, or no lines as in cool helium atmospheres (Kawka & Vennes 2014; Hollands et al. 2015). Nevertheless, if there is a link between the debris observed to pollute white dwarf atmospheres, and the prevalence or strength of stellar magnetic fields, it would suggest that closely orbiting planets or their engulfment during a common envelope can generate sustained (weak) magnetism in white dwarfs (Farihi et al. 2011; Kissin & Thompson 2015).

This process would be a planetary-mass analogue to strong magnetic field generation via mergers and common envelope evolution of stellar-mass companions (Tout et al. 2008; Nordhaus et al. 2011). The results discussed below are the part of a concerted effort to determine the frequency of weak magnetic fields among polluted white dwarfs.

For the measurements and upper limits obtained, a tilted and centred magnetic dipole will have a surface polar field strength that is related to the maximum observed value of the surface-averaged field by the following inequality (Aurière et al. 2007)

$$B_* \gtrsim 3.3 \, \langle B_z \rangle_{\max}. \qquad (2)$$

This is useful in the case where multi-epoch detections and stellar rotation rates are not available, as in this study. Thus a lower limit on the surface dipole component of the magnetic field can be estimated from circular spectropolarimetry.

0322–019. This star was first shown to be weakly magnetic via Zeeman splitting in multiple metal and Hα in an optical spec-

trum with resolving power $R \approx 40\,000$ and S/N ≈ 100 (Farihi et al. 2011). The nature of the weak splitting due to a $B_* \approx 120$ kG field only became apparent within a combined data set consisting of two dozen individual, co-added spectra which totaled 6.0 h of exposure. The Ca II splitting had been previously detected in high-resolution data, but attributed to binarity (Zuckerman et al. 2003). Fig. 1 plots the second data set of spectropolarimetry for this white dwarf, and shows that P_v is clearly non-zero. Although the Zeeman splitting is unresolved in the FORS2 Stokes *I* spectra, this magnetic field detection was achieved in just over 20 min of on-source time (cf. the UVES detection). P_v was determined only from the region of Ca II H, K, and Ca I 4226 Å. The surface-averaged, longitudinal field detected is 16.5 ± 2.3 kG, which is a factor of several smaller than the intrinsic field strength estimated from Zeeman splitting, and thus consistent with equation (2). The first observation of this star did not result in a detection and is likely due to a chance alignment with the magnetic equator.

1145+017. There are four relatively deep observations of this iconic source, but only in the third data set is there potentially real signal. However, as discussed in Section 2.1, anything below 5σ cannot be viewed as a confident detection and hence the 3.5σ result for the third epoch should be viewed as a promising result that requires confirmation with additional observations. The third data set for this star is plotted in Fig. 1 and shows the weak but non-zero slope in P_v. Adopting $\langle B_z \rangle_{\max} \approx 1$ kG, then the minimum dipolar field strength would be 3 kG.

It is important to place the best possible constraint on the magnetic field of this star for the X-ray analysis that follows. In order to complement the limits provided by circular spectropolarimetry, the published HIRES spectrum with resolving power $R \approx 40\,000$ (Xu et al. 2016) was examined for any indication of Zeeman splitting. While none is evident, a series of model stellar atmospheres with increasing magnetic field strength was generated in order to place upper limits via the absence of Zeeman-split lines. The LLMODELS stellar atmosphere code (Shulyak et al. 2004) was used, together with the published stellar parameters abundances. From this baseline model atmosphere, synthetic Stokes *I* stellar spectra were computed using the SYNMAST code (Kochukhov, Makaganiuk & Piskunov 2010), for purely radial (dipolar) magnetic fields of increasing strength. The data and models are shown in Fig. 4 for two narrow wavelength regions with strong photospheric lines of Mg II and Si II that are well isolated from circumstellar, as well as additional stellar absorption. The results of the magnetic modelling indicate that fields as large as 30 kG would be obvious, and hence a more realistic upper limit is $B_* < 20$ kG.

1929+011. The highly polluted and $T_{\rm eff} \approx 21\,000$ K white dwarf has no previous observations using circular spectropolarimetry. The single observational limit here is not highly constraining, but taken at face value suggests that a dipolar field on the order of tens of kG remains possible. High-resolution UVES spectra of this star exist (Vennes, Kawka & Németh 2010), which have nearly identical resolving power ($R \approx 40\,000$) to the HIRES data analysed above. Modelling similar to that performed for 1145+017 was carried out on the UVES data for the strong Mg II 4482 Å feature (not shown), and a similar upper limit of 20 kG is estimated.

2105–820. This star was a magnetic suspect first identified during a search for rotational broadening in the NLTE cores of Hα, where it shows a clearly flattened core shape consistent with a $B_* = 43$ kG intrinsic field (Koester et al. 1998). This has been confirmed with higher resolution data taken with UVES for the SPY survey (Koester et al. 2009), where it also exhibits a flattened core in the weak
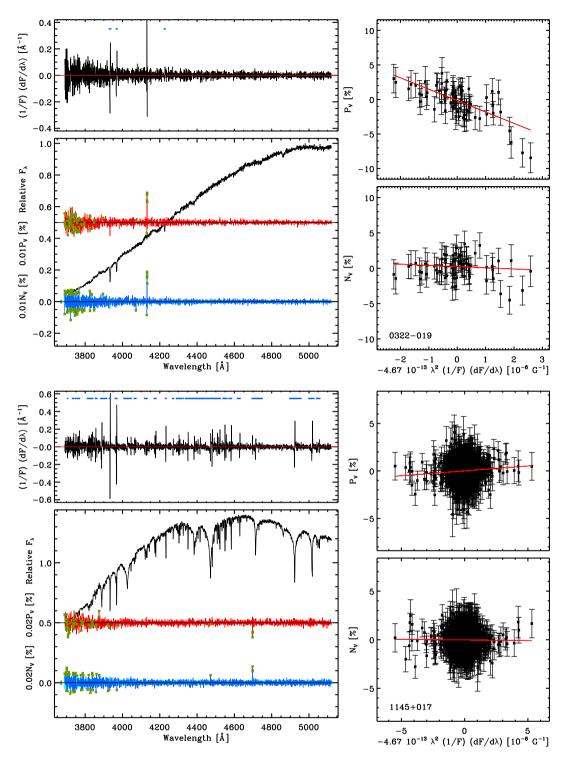
Figure 1. Plots of spectropolarimetric data where the fractional polarization is greater than $3\sigma - 5\sigma$ (see Section 2.1 and boldface numbers in Table 1 column ten). Each group of four plots corresponds to a single observational data set for one star. The upper left panels plot the derivative of the slope for each spectrum in black, with blue dashes marking the regions used to determine $P_v = V/I$. The lower left panel shows the relative Stokes I (total flux) spectrum in black, with P_v and N_v plotted against wavelength in red and blue respectively. Green crosses label data points that were removed from analysis via sigma clipping of outliers from the local average (i.e. cosmic rays, detector artefacts, noisy regions). The right-hand panels plot P_v and N_v as a function of the right-hand side of equation (1), where the red lines have been determined by least squares fitting, and the resulting slopes are exactly $\langle B_z \rangle$ and $\langle N_z \rangle$ respectively.

but clearly detected Ca II K absorption line (Koester et al. 2005), demonstrating that the metal is unambiguously photospheric.

This white dwarf was previously detected in circular polarization over the higher Balmer lines, where five detections were ob-

tained for surface-averaged fields in the range 8–11 kG (Landstreet et al. 2012). The data over the H α region are shown in Fig. 1 and are consistent with a longitudinal field of 5 kG, which is roughly half that detected consistently over several days and longer by
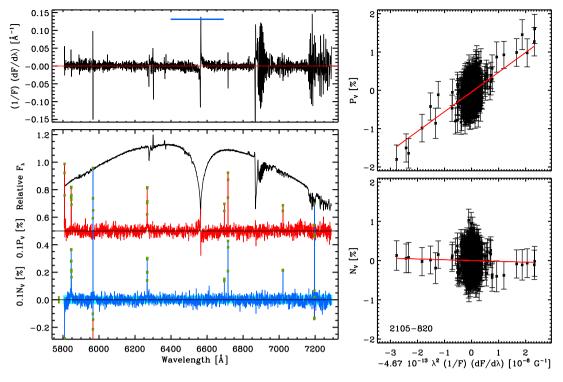
Figure 1 – *continued*

Landstreet et al. (2012) using FORS1. This discrepancy is not actually meaningful, however, as studies have shown that even within a single instrument, each specific grating and wavelength setting define a specific instrumental system for measuring $\langle B_z \rangle$ (Landstreet, Bagnulo & Fossati 2014). Owing to various differences induced by individual setups, measurements made with different systems are not directly comparable except for general magnitude. Nevertheless, the field detected via Hα spectropolarimetry leads to a lower limit on the dipolar magnetic field strength of roughly 17 kG (equation 2), which is consistent with the $B_* = 43$ kG estimated from Zeeman splitting.

2326+049. This is one of the most well-studied degenerate stars known and is the prototype dusty and polluted white dwarf (Zuckerman & Becklin 1987; Koester, Provencal & Shipman 1997). Circular spectropolarimetry was performed on this target over two decades prior, resulting in a non-detection with a 5σ error of 64 kG (Schmidt & Smith 1995). Table 1 indicates that the FORS2 5σ upper limit is 2.5 kG, consistent with both $\langle B_z \rangle$ and $\langle N_z \rangle$ and their dispersions. As with the other stars in the sample, 2326+049 also has high-resolution optical spectra that can be used to place magnetic field limits via the absence of Zeeman splitting. Using the same methodology as above for Ca II 3968 Å (not shown), an upper limit field strength of 20 kG is estimated, consistent among all the stars with similarly high-resolution spectral data.

Although spectropolarimetry was not obtained for 1729+371, a similar estimate of $B_* < 20$ kG is adopted, as this polluted white dwarf also has $R \approx 40\,000$ HIRES data with no evidence of Zeeman splitting (Zuckerman et al. 2007).

3.2 Interpretation of X-ray upper limits

This section presents a theoretical framework in which to interpret the X-ray upper limits at polluted white dwarfs including 1145+017. The Alfvén radius for a gas disc accreting at a rate

$\dot{M} = \dot{M}_{10} \times 10^{10}$ g s^{-1} is given by (e.g. Ghosh & Lamb 1978)

$$R_A = \left(\frac{3 B_*^2 R_*^6}{2 \dot{M} \sqrt{G M_*}} \right)^{2/7} \approx 0.52\, R_\odot \left(\frac{B_*}{\text{kG}} \right)^{4/7} \dot{M}_{10}^{-2/7}, \qquad (3)$$

where B_* is the surface polar magnetic field strength of a white dwarf with assumed mass $M_* = 0.6\,M_\odot$ and radius $R_* = 9.0 \times 10^8$ cm. Fig. 5 plots R_A as a function of accretion rate for a range of magnetic field strengths representative of detections and upper limit estimates for the observed sample. Thus, for the ongoing accretion rates thought to be characteristic of polluted white dwarfs, the Alfvén radius will reside near or exterior to the Roche radius (Metzger et al. 2012), and further outside of where the disc becomes dominated by (sublimated) gas. Furthermore, R_A will remain well above the stellar surface unless the star is essentially non-magnetic and $B_* < 1$ G, or the accretion rate is extreme at $\dot{M} > 10^{16}$ g s^{-1}.

For typical (single) white dwarfs, rotation periods $2\pi/\Omega_*$ are many hours to days (Hermes et al. 2017), and hence the co-rotation radius $R_c = (G M_*/\Omega_*^2)^{1/3}$ will also be outside the expected radius of the gas disc. The accretion flow should therefore divert on to the stellar magnetosphere near the radius R_A (without a propellor), interior to which matter will be placed on to field lines leaving the magnetic polar region at a characteristic latitude $\theta_m \approx \sin^{-1}(\sqrt{R_*/R_A}) \approx \sqrt{R_*/R_A}$. The accretion column will therefore cover a fraction of the stellar surface crudely given by

$$f_m = \frac{2\pi \theta_m^2}{4\pi} \approx \frac{1}{2} \frac{R_*}{R_A} \approx 0.013 \left(\frac{B_*}{\text{kG}} \right)^{-4/7} \dot{M}_{10}^{2/7}. \qquad (4)$$

This expression assumes a magnetic axis aligned with the disc angular momentum, where a large misalignment will decrease f_m by factors of order unity. Furthermore, observations of X-ray emitting spots on white dwarfs demonstrate that the accretion geometry can be substantially more complex than this (see Mukai 2017, and references therein). Nevertheless, equation (4) serves as a useful
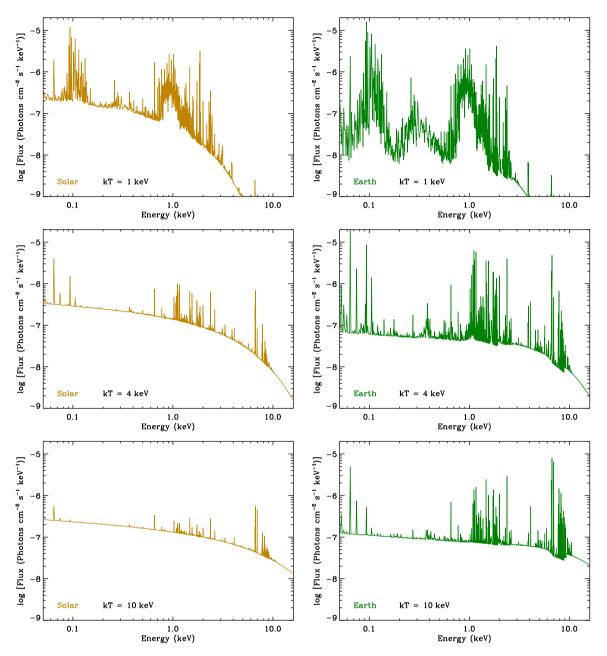
Figure 2. Output of XSPEC simulations run for solar (gold) and bulk Earth (green) composition plasmas of temperature 1, 4, and 10 keV. Each of the plots has been normalized to match the MOS upper limit fluxes of WD 1145+017. The logarithmic scale emphasizes that the emergent flux is generally dominated by line emission, especially for lower temperatures and Earth composition gas. These results support the analytical model (Section 3.2) in which line emission – from Fe in particular – dominates the X-ray flux in the range $kT \simeq 1 - 10$ keV.

first approximation for the fraction of the stellar surface subject to accretion infall.

Matter falling onto the polar cap will have free-fall velocity $v_{\mathrm{ff}} \approx \sqrt{2GM_*/R_{\mathrm{sh}}} \approx \sqrt{GM_*/R_*} \approx 3000\,\mathrm{km\,s^{-1}}$, where the shock radius R_{sh} is taken to be twice the stellar radius. Given the range of relevant accretion rates, the shock will be adiabatic and thus not immediately collapse into a thin radiative shock close to the stellar surface. The infalling gas will be shock-heated to a temperature

$$kT_{\mathrm{sh}} \approx \frac{3}{16}\mu m_{\mathrm{p}} v_{\mathrm{ff}}^2 \approx \frac{3}{8}\frac{GM_* m_{\mathrm{p}}}{R_*} \approx 37\,\mathrm{keV}, \qquad (5)$$

where $\mu \approx 2$ is the mean molecular weight for fully ionized matter

of bulk Earth composition. The post-shock gas will be compressed to a density of

$$\rho_{\mathrm{sh}} \approx \frac{\dot{M}}{\pi R_{\mathrm{sh}}^2 f_{\mathrm{m}} v_{\mathrm{ff}}} \approx 3.6 \times 10^{-16} \dot{M}_{10} \left(\frac{f_{\mathrm{m}}}{0.01}\right)^{-1}\,\mathrm{g\,cm^{-3}}. \qquad (6)$$

Gas will cool behind the shock radiatively at approximately constant pressure $P \propto \rho T$. Thus, neglecting recombination effects, as the gas cools to temperature T from its initial T_{sh} (equation 5), it will compress according to

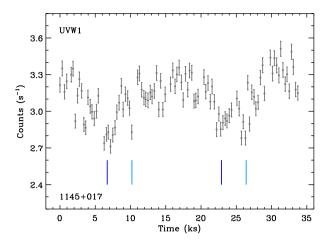$$T\rho = T_{\mathrm{sh}}\rho_{\mathrm{sh}}. \qquad (7)$$

Figure 3. Optical monitoring data from *XMM* covering the first 35 ks of the X-ray observations for 1145+017 using the *UVW*1 filter. The raw data were sampled at 10 s, but have been re-binned in the plot to 300 s to reduce noise and reveal structure in the crude light curve. There are two broad sets of depressions in counts, with potentially two sub-structures each marked in dark and light blue, where these pairs are roughly separated by 4.5 h = 16.2 ks. It is difficult to establish a baseline flux from these data, but the peak-to-trough distance is 23 per cent of the peak value, consistent with dimming activity throughout the X-ray exposure.

In order to settle onto the stellar surface, the gas must release a total radiative luminosity of

$$L_{\text{tot}} = \frac{GM_*\dot{M}}{R_*} \approx 8.9 \times 10^{26} \dot{M}_{10} \text{ erg s}^{-1}. \quad (8)$$

Three gas cooling mechanisms within the accretion column will determine the wavelength regimes for this emission: (1) bremsstrahlung (free–free emission), (2) atomic (i.e. line) emission, and (3) cyclotron emission. The cooling rate per unit volume is commonly written as $\dot{q} = -n^2\lambda$, where $n \equiv \rho/m_p$ and λ is the cooling function. Cooling rates in general will differ from that of solar metallicity gas due to the distinct composition of the accreting (planetary) matter, and here is taken as bulk Earth (McDonough 2000), as is observed to dominate the heavy element mass in more than one dozen white dwarfs with detailed measurements (Jura & Young 2014).

At low temperatures and high density, atomic cooling will predominate. Fig. 6 shows the atomic cooling rate for bulk Earth composition, calculated assuming collisional ionization equilibrium and fully ionized gas (a reasonable approximation at the high temperatures of interest) from Schure et al. (2009). Owing to the large number of atomic transitions, cooling from Fe will determine the total cooling rate across all temperatures of interest, which also greatly exceeds the free–free cooling rate.

However, at low densities and high temperatures, cyclotron cooling can dominate over atomic cooling if the magnetic field is sufficiently strong. The cyclotron cooling rate behind the shock near the stellar surface is approximately given by

$$\Lambda_{\text{B}} \approx \frac{3}{2}\frac{\sigma_T}{c}\frac{B_{\text{sh}}^2}{8\pi}\frac{m_p}{m_e}\left(\frac{kT}{\rho}\right) = \frac{3B_*^2}{128\pi}\frac{\sigma_T}{c}\frac{m_p}{m_e}\left(\frac{kT_{\text{sh}}}{\rho_{\text{sh}}}\right)\left(\frac{T}{T_{\text{sh}}}\right)^2$$

$$\approx 5 \times 10^{-20} \dot{M}_{10}^{-1}\left(\frac{f_m}{0.01}\right)\left(\frac{B_*}{\text{kG}}\right)^2\left(\frac{T}{T_{\text{sh}}}\right)^2 \text{ erg cm}^3 \text{ s}^{-1}$$

$$\approx 6 \times 10^{-20} \dot{M}_{10}^{-5/7}\left(\frac{B_*}{\text{kG}}\right)^{10/7}\left(\frac{T}{T_{\text{sh}}}\right)^2 \text{ erg cm}^3 \text{ s}^{-1}, \quad (9)$$
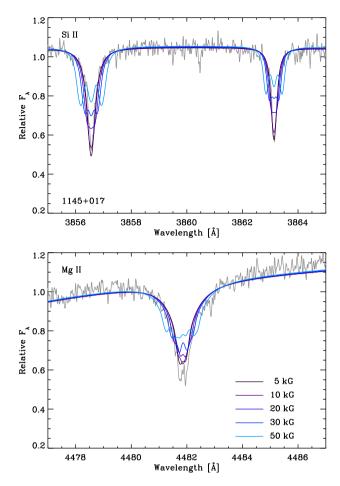

Figure 4. Magnetic stellar atmosphere models used to estimate an upper limit to the mean magnetic field modulus for an intrinsic (dipolar) field for 1145+017. Keck HIRES data with resolving power $R \approx 40\,000$ (Xu et al. 2016) are shown in grey for two regions containing the strongest metal absorption features that are purely photospheric, and where the lines are isolated from other (atmospheric and circumstellar) absorbers. A synthetic stellar spectrum was modified for purely radial field strengths of $B_* = 5$, 10, 20, 30, and 50 kG (Kochukhov et al. 2010) with the resulting spectra overplotted as the colours shown in the legend. These model spectra indicate that the effects of Zeeman splitting should have been observed for field strengths above 20 kG.

where σ_T is the Thomson cross-section. In the second and final lines, equations (6) and (7) have been used and in the final line f_m has been substituted from equation (4). The magnetic field strength B_{sh} behind the shock at $r \approx 2R_*$, is assumed to be eight times lower than the surface value B_* due to the $\propto 1/r^3$ dilution for a dipole field.

Fitting the atomic cooling rate to a power law of $\Lambda = 1.0 \times 10^{-23}(kT/10 \text{ keV})^{-0.8} \text{ erg cm}^3 \text{ s}^{-1}$, versus the comparatively sensitive temperature dependence of $\lambda_B \propto T^2$, we estimate that cyclotron cooling will dominate above a critical temperature

$$T_{\text{B}} \approx 1.1 \dot{M}_{10}^{0.26}\left(\frac{B_*}{\text{kG}}\right)^{-0.51} \text{ keV}. \quad (10)$$

In cases, when $T_{\text{sh}} \gtrsim T_{\text{B}}$ it is expected that only a fraction $\sim T_{\text{B}}/T_{\text{sh}}$ will emerge as line emission at temperatures $T \lesssim T_{\text{B}}$. Translating to the regime of interest for the *XMM* observations, the total X-ray luminosity (when $T_{\text{B}} \lesssim T_{\text{sh}} \approx 37$ keV) will be given by

$$L_{\text{X}} = \frac{T_{\text{B}}}{T_{\text{sh}}}L_{\text{tot}} \approx 3 \times 10^{25} \dot{M}_{10}^{1.26}\left(\frac{B_*}{\text{kG}}\right)^{-0.51} \text{ erg s}^{-1}. \quad (11)$$
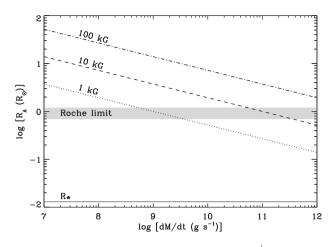
Figure 5. Alfvén radius as a function of gas accretion rate $\dot{M}$ from equation (3) for white dwarfs with fixed magnetic field strengths of $B_* = 1$, 10, and 100 kG. Shown for comparison is a grey region whose height corresponds to the full range of Roche radii for asteroids of mean density $\rho = 1$–5 g cm^{-3}. Magnetic fields as weak 1 kG or weaker will have a profound effect on the behaviour of gas interior to 1 R$_\odot$ when $\dot{M} \lesssim 10^{10}$ g s^{-1}, and especially as the material accretes within several R_*.

Table 3. Benchmark X-ray luminosity and accretion rate limits.

kT	L_X	$\dot{M}\,(B_* = 1\,\text{kG})^a$	$\dot{M}\,(B_* = 0)^b$
(keV)	(10^{27} erg s^{-1})	— (10^{10} g s^{-1})	
		1145+017 (174 pc)	
1	2.1	50	4.7
4	4.3	89	9.7
10	8.7	160	20
		1729+371 (50.6 pc)	
1	0.3	12	0.8
4	0.8	24	1.9
10	1.8	44	4.0
		2326+049 (17.6 pc)	
1	0.2	7.0	0.4
4	0.4	14	0.9
10	0.8	24	1.9

Notes. [a] Using equation (11).
[b] Using equation (8).
All values are for accreting material of bulk Earth composition. L_X is the bolometric luminosity due to accretion, while $\dot{M}$ accounts for the fact that half of L_X is directed back into the star.
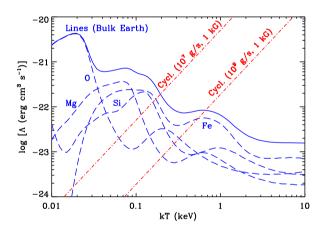

Figure 6. Cooling function Λ for different processes in the accretion column as a function of the gas temperature. Atomic cooling rates for fully ionized matter with bulk Earth composition (McDonough 2000) are shown with blue lines; dashed curves show the contributions of individual elements and a solid line shows the total cooling rate. Dot–dashed red curves show the cyclotron cooling rate for different assumptions about accretion rate $\dot{M} = 10^7$ and 10^9 g s^{-1}, for an assumed surface magnetic field strength of $B_* = 1$ kG.

The remaining luminosity will emerge as cyclotron emission, at much lower radio frequencies of

$$\nu \gtrsim \frac{eB_*}{2\pi m_e c} \approx 3 \left(\frac{B_*}{\text{kG}} \right) \text{GHz.} \tag{12}$$

Any cyclotron radiation has a maximum flux density set by the blackbody equivalent at T_{sh}. As flux scales linearly with temperature in the Rayleigh–Jeans regime, the most optimistic cyclotron flux can only be $T_{\text{sh}}/T_{\text{eff}} \sim 10^4$ times brighter than the stellar photosphere. This puts optimistic radio fluxes in the nJy range for typical white dwarfs and thus not detectable with current radio facilities.

3.3 Upper limit accretion rates

Upper limit accretion rates were calculated for the three X-ray observed white dwarfs in two regimes: where weak magnetic fields of order 1 kG may play a role equation (11) was used, and a non-magnetic calculation was done using equation (8). As the temperature of the emission is empirically unconstrained, both X-ray luminosity and accretion rate limits were derived for the full range of kT considered here. Calculations were based on the model spectra for material with bulk Earth composition, and the most stringent bolometric X-ray flux constraint for each kT value was taken as input (e.g. the 0.3–2.0 keV energy range limits for $kT = 1$ keV). Upper bound, total X-ray fluxes were transformed into luminosities using the best available distance estimate for 1145+017 (174 pc; Vanderburg et al. 2015), and the most recent parallaxes for 1729+371 (50.6 pc; Kilic, Thorstensen & Koester 2008) and 2326+049 (17.6 pc; Subasavage et al. 2017). The calculated upper limit X-ray luminosities and mass accretion rates are given in Table 3, with L_X values listed as totals, whereas $\dot{M}$ limits account for half the luminosity being directed away from the observer.

1145+017. Unless this star has a magnetic field strength that is significantly greater than 1 kG, then the accretion rate based on the models presented here cannot be as high as 10^{12} g s^{-1}. Furthermore, if the white dwarf is essentially non-magnetic, then the current accretion rate should be less than 10^{11} g s^{-1} and thus consistent with the rate inferred from the atmospheric metal abundances under the assumption of a steady-state balance between accretion and diffusion. However, 1145+017 has an atmosphere dominated by helium, where a typical heavy element persists for several 10^5 yr (Koester et al. 2009) before fully sinking below the outer layers, and thus a steady-state is far from certain. The current accretion rate could be significantly lower than the upper limits broadly set by the X-ray data and modelling, and even lower than more modest rates of order 10^{10} g s^{-1} for a steady-state accretion regime.

These findings are also consistent with an ongoing accretion rate below all the above estimates, and potentially on the order of 10^8–10^9 g s^{-1}, which represent the upper end of rates confidently

inferred to be ongoing for white dwarfs with infrared excess (Bergfors et al. 2014). Nevertheless, the current mass of atmospheric metals divided by their sinking time-scale does give a historical average rate of accretion over the past diffusion time-scale, and in the case of 1145+017 suggests the system experienced some higher rate episode(s) within the past Myr (Girven et al. 2012), where these are likely short-lived and stochastic events (Farihi et al. 2012; Wyatt et al. 2014). Overall, these results support the possibility that 1145+017 is a relatively ordinary dusty and polluted white dwarf, but with a particular viewing geometry that reveals a spectacular light curve and absorption spectrum.

1729+371 and 2326+049. The results presented here for these two stars can be compared directly with a previously published analysis of their *XMM* data, where Jura et al. (2009) find upper limit accretion rates of $2 \times 10^{10}\,\mathrm{g\,s^{-1}}$ and $2 \times 10^{9}\,\mathrm{g\,s^{-1}}$, respectively. There are several noteworthy differences between the approach taken by that study, and the data and modelling done here. First, upper bound count rates were converted to fluxes using PIMMS as opposed to the more sophisticated XSPEC analysis done here, where the former is restricted to solar ratios of the elements. Secondly, any interstellar absorption was ignored (however, this simplification is probably fine as both stars are within the Local Bubble), but is accounted for in Table 3. Thirdly, in the previous study the bolometric corrections to the observed flux limits were made by assuming the accretion luminosity emerges solely as high-energy radiation (i.e. no stellar magnetism or cyclotron radiation), with half of the photons directed towards an observer, and half of these within the *XMM* bandpasses. Here, XSPEC was used to construct a bolometric flux F for each star and model, and these have been converted to luminosity using $L = F \times 4\pi d^2$, where d is the distance to each star.

Given these potentially significant differences, it is perhaps surprising that the accretion rate limits reported by Jura et al. (2009) are comparable to the values listed in the fourth column of Table 3. For 1729+371, the upper bound counts of both studies are identical, and the non-magnetic limits calculated here are a match at 4 keV. Both sets of results are consistent with an ongoing accretion rate comparable to warm DAZ stars – where a steady state is likely, and accretion rates can be inferred with confidence from metal abundances – and no more than a few times $10^9\,\mathrm{g\,s^{-1}}$ (Farihi et al. 2012).

However, for 2326+049 the non-magnetic limits on accretion rate found here for 4 keV are roughly a factor of three larger than those reported by Jura et al. (2009), reflecting the fact that their upper bound count rates are a factor of three smaller than those listed in Table 2. Consistent with this, their limiting fluxes for this source are a factor of a few smaller than the in-band flux values listed in Table 2. As mentioned in Section 2.2, no attempt was made here to remove or model the nearby X-ray source whose flux contaminated the aperture used to derive the upper bound counts here.

If the factor of a few difference between the studies is taken at face value, and is an accurate reflection of the upper bounds to the counts from 2326+049 (based on undocumented but accurate corrections made by Jura et al. 2009), then that would fold into the upper limit accretion rates derived here. A factor of three fewer in counts would translate into commensurately lower X-ray luminosities and accretion rate limits. Xu et al. (2014) derive a steady-state accretion rate of $6.5 \times 10^8\,\mathrm{g\,s^{-1}}$ for 2326+049 based on the detection of eight heavy elements, while the non-magnetic Table 3 values made smaller by a factor of three would yield a range of $1 - 6 \times 10^9\,\mathrm{g\,s^{-1}}$. While these values are all potentially consistent, it raises the possibility that accretion luminosity from 2326+049 may be detectable with a deep X-ray pointing.
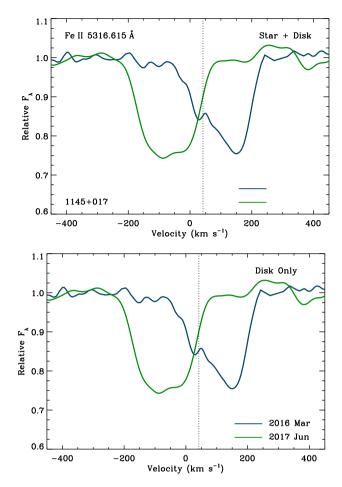

Figure 7. Two epochs of spectroscopy for 1145+017 in the vicinity of the Fe II 5316 Å line, separated by 1.3 yr. VLT X-shooter data taken in 2016 March are plotted in dark blue, and Keck HIRES spectra taken in 2017 June are shown in green and have been re-binned to match the resolution of the X-shooter data. The top panel shows the combined and normalized spectra as obtained, while the stellar atmosphere has been removed from the data shown in the bottom panel (Redfield et al. 2017), and the dotted lines denote the photospheric velocity. The clear variation in disc geometry indicates that the red-shifted gas seen in 2015 and 2016 is not in the process of accreting into the star at the observed velocities, and hence the high accretion rate calculated for this star based on the circumstellar gas mass and velocity (Xu et al. 2016) is unlikely.

3.4 Additional Constraints on Accretion in 1145+017

As part of an ongoing program to monitor the circumstellar absorption features seen in optical spectra of 1145+017, Keck HIRES data were taken on 2017 June 27. The data were taken and reduced in a manner identical to that described in detail in Redfield et al. (2017). A portion of these recent HIRES data are displayed in Fig. 7, in the region surrounding the strong circumstellar absorption feature from Fe II 5316Å, and plotted alongside similar data taken 15 months prior. As can be seen from these two sets of spectra, the distribution of velocities of the circumstellar gas has changed dramatically, and the gas does not appear to be infalling.

Redfield et al. (2017) showed the circumstellar gas disc orbiting 1145+017 had an inner edge in the range $60 - 80\,R_*$ that was nearly constant from 2015 November to 2016 April, and one possible explanation was disc truncation due to a magnetic field. While this possibility is consistent with the range of allowed R_A (see Fig. 5) and the results found here using spectropolarimetry, Redfield et al.

(2017) concluded that the magnetospheric accretion model could not account for the particular shape of the observed circumstellar gas line profiles as well as the necessary ring eccentricity.

The *XMM* observations of 1145+017 were designed to test the magnetospheric truncation possibility, as this model contains analytical relationships between the observed gas velocity distribution via absorption, accretion rate and magnetic field at a given orbital radius. This model predicted a range of accretion rates for 1145+017 in the range 2×10^{11}–5×10^{12} g s^{-1}, which are clearly ruled out by the X-ray data. The new epoch of HIRES data also supports a gas disc behaviour that is not strongly influenced by a magnetosphere via truncation at the inner edge, and which is also consistent with the upper limit magnetic field estimates from both the absence of Zeeman splitting and spectropolarimetry.

4 DISCUSSION AND CONCLUSIONS

4.1 Accretion overview

There are currently few empirical constraints on the exact behaviour of gas and dust – production, evolution, and eventual accretion – within planetary debris discs orbiting white dwarfs. Specifically, there are no direct measurements of instantaneous accretion rate, only inferences based on the mass of atmospheric metals in stars where a steady-state is likely due to sinking time-scales $t \ll 100$ yr. While these inferred, ongoing rates are limited to rates on the order of 10^9 g s^{-1} and lower, there is compelling evidence for historical rates up to several orders of magnitude higher (Farihi et al. 2012), based on the time-averaged accretion rates for those stars with sinking time-scales up to order Myr (Girven et al. 2012). Any high-rate episodes must necessarily be short-lived to be consistent with the lack of detection among hundreds of stars where a steady-state regime is favoured (Koester et al. 2005; Girven et al. 2011).

Models for accretion on to polluted white dwarfs have demonstrated that Poynting–Robertson (PR) drag provides the rate bottleneck for a disc dominated by particles (Rafikov 2011). Moreover, the infall rates predicted by modelling of *optically thick* discs are in excellent agreement with those inferred for systems likely to be accreting in a steady state (Farihi 2016). In contrast, the accretion rate predictions for *optically thin* discs are at best a factor of 10^2 lower than that inferred from observational data (Bochkarev & Rafikov 2011). However, if an optically thin cloud or shell has significant vertical extent where all particles are unobscured and directly illuminated by starlight, then $\dot{M} = \tau L_*/c^2$, where τ is the fraction of intercepted starlight (Metzger et al. 2012), and this formulation appears consistent with the vertical extent estimated for the circumbinary material polluting SDSS J155720.77+091624.6 (Farihi, Parsons & Gänsicke 2017a).

The presence and generation of gas within a disc can strongly influence the evolution and accretion rate, especially in the regimes of a completely gaseous disc, where the viscous spreading time-scale can be orders of magnitude shorter than that for PR drag on dust (Jura 2008), or one where particles are strongly coupled to the gas (Metzger et al. 2012). In such cases, it has been speculated that accretion rates can soar to 10^{11} g s^{-1} or possibly even higher (Bear & Soker 2013). Although a small sample of three systems, neither X-ray data nor steady-state rates inferred from metal abundances have yet to detect such high-rate accretion.

Recently, Kenyon & Bromley (2017) have modelled a narrow and mildly eccentric annulus containing a swarm of debris particles that undergo a collisional cascade. In contrast to other disc models, the collisional cascade produces discs with large vertical heights

that are up to several times the stellar radius, and accretion rates that can exceed 10^{11} g s^{-1} by up to two orders of magnitude, and persist for time-scales up to 10^4 yr. This collisional disc model thus requires replenishment on time-scales where the cascade depletes the disc, and this could be accomplished with the stochastic infall of planetesimals as described by Wyatt et al. (2014).

Overall, this study finds no evidence for accretion rates exceeding the 10^8–10^9 g s^{-1} inferred by steady-state calculations, but a larger sample of X-ray observations would provide better constraints on instantaneous accretion rates.

4.2 Results summary

Using circular spectropolarimetry, robust detections of magnetic fields are found for 0322–019 and 2105–820, supporting earlier estimates from Zeeman splitting in dipole fields of $B_* \approx 120$ and 40 kG, respectively. Neither of these polluted white dwarfs has an infrared excess, and while this is consistent with their Alfvén radii being larger than their Roche radii, it is not necessarily the case that the absence of infrared disc emission is due to magnetospheric disc truncation. In the case of 0322–019 with $T_{\rm eff} \approx 5300$ K, this star sits among a large class of metal-lined white dwarfs older than 0.5 Gyr, where infrared excesses are rarely observed (Xu & Jura 2014; Bergfors et al. 2014), and in which the heavy element sinking time-scales are sufficiently long that accretion may have ended. For 2105–820, it has a steady-state accretion rate of 3×10^7 g s^{-1} based on its calcium abundance, and likely below the ability of space- and ground-based detection of its disc (Rocchetto et al. 2015; Bonsor et al. 2017).

While there is a tentative indication of a spectropolarimetric signal from 1145+017, additional confirmation is necessary. The high-resolution spectral modelling of several metal lines where Zeeman splitting is absent suggests the field cannot be larger than around 20 kG, and similarly for 1929+011 and 2326+049 based on comparable analyses of archival spectra. Thus it appears the magnetically trapped dust model of Farihi et al. (2017b) is likely ruled out in the case of the observed dimming events towards 1145+017. Further searches for weak magnetic fields in polluted white dwarfs can assess the applicability of this model in other systems.

The study aimed to probe the role of magnetic fields in either the evolution of dust or its eventual accretion onto the surface of white dwarfs such as 1145+017, and to directly detect any accretion luminosity. In the case of 1145+017, several favourable estimates have been given in the literature ranging from 10^{10} g s^{-1} to 10^{12} g s^{-1} (Vanderburg et al. 2015; Gänsicke et al. 2016; Rappaport et al. 2016; Xu et al. 2016). As there is no confident indication of magnetic fields in the X-ray observed sample, upper limit accretion rates are taken in the non-magnetic regime and appear to support none of the above estimates. Rather, as discussed above, the spectacular nature of 1145+017 appears to be its geometry, not its accretion rate. If correct, the underlying parent body or bodies inferred to be orbiting near 4.5 h may be undergoing *collisions* rather than disintegration, as the latter implies the system is observed at a special time, which may not be the case.

For 2326+049 the upper limit $\dot{M}$ values are consistent with that derived by Xu & Jura (2014) for steady-state accretion, or several times 10^8 g s^{-1}. This is tantalizingly close to the most favourable X-ray limit if the upper bound count rate reported by Jura et al. (2009) is more accurate than that estimated here. It is noteworthy that such a rate is consistent with predictions for optically thick disc models, and also the case where an optically thin disc has a significant vertical height and intercepts several percent of incident

starlight. However, in this case micron-sized disc particles should have been consumed by PR drag since its discovery (Zuckerman & Becklin 1987), unless they are being replenished.

REFERENCES

Angel J. R. P., Landstreet J. D., 1970, ApJ, 160, L147
Appenzeller I. et al., 1998, Msngr, 94, 1
Asplund M., Grevesse N., Sauval A. J., Scott P., 2009, ARA&A, 47, 481
Aurière M. et al., 2007, A&A, 475, 1053
Bagnulo S., Szeifert T., Wade G. A., Landstreet J. D., Mathys G., 2002, A&A, 389, 191
Bagnulo S., Landstreet J. D., Fossati L., Kochukhov O., 2012, A&A, 538, A129
Bagnulo S., Fossati L., Kochukhov O., Landstreet J. D., 2013, A&A, 559, A103
Baskill D. S., Wheatley P. J., Osborne J. P., 2005, MNRAS, 357, 626
Bear E., Soker N., 2013, New Astron., 19, 56
Bergfors C., Farihi J, Dufour P., Rocchetto M., 2014, MNRAS, 444, 2147
Bochkarev K. V., Rafikov R. R., 2011, ApJ, 741, 36
Bonsor A., Farihi J., Wyatt M. C., van Lieshout R., 2017, MNRAS, 468, 154
Chauvin G. et al., 2017, A&A, 605, L9
Donati J. F. Semel M., Carter B. D., Rees D. E., Collier Cameron A., 1997, MNRAS, 291, 658
Farihi J., 2016, New Astron. Rev., 71, 9
Farihi J., Zuckerman B., Becklin E. E., 2008, ApJ, 674, 431
Farihi J., Barstow M. A., Redfield S., Dufour P., Hambly N. C., 2010, MNRAS, 404, 2123
Farihi J., Dufour P., Napiwotzki R., Koester D., 2011, MNRAS, 413, 2559
Farihi J., Gänsicke B. T., Wyatt M. C., Girven J., Pringle J. E., King A. R., 2012, MNRAS, 424, 464
Farihi J., Parsons S. G., Gänsicke B. T., 2017a, Nature Astron., 1, 32
Farihi J., von Hippel T., Pringle J. E., 2017b, MNRAS, 471, L145
Fossati L. et al., 2015, A&A, 582, A45
Gänsicke B. T., Koester D., Farihi J., Girven J., Parsons S. G., Breedt E., 2012, MNRAS, 424, 333
Gänsicke B. T. et al., 2016, ApJ, 818, L7
Ghosh P., Lamb F. K., 1978, ApJ, 223, L83
Girven J., Gänsicke B. T., Steeghs D., Koester D., 2011, MNRAS, 417, 1210
Girven J., Brinkworth C. S., Farihi J., Gänsicke B. T., Hoard D. W., Marsh T. R., Koester D., 2012, ApJ, 749, 154
Gurri P., Veras D., Gänsicke B. T., 2017, MNRAS, 464, 321
Hermes J J. et al., 2017, ApJ, 841, L2
Hollands M. A., Gänsicke B. T., Koester D., 2015, MNRAS, 450, 681
Jura M., 2003, ApJ, 584, L91
Jura M., 2008, ApJ, 135, 1785
Jura M., Young E. D., 2014, AREPS, 42, 45
Jura M., Muno M. P., Farihi J., Zuckerman B., 2009, ApJ, 699, 1473
Kawka A., Vennes S., 2014, MNRAS, 439, L90
Kawka A., Vennes S., Schmidt G. D., Wickramasinghe D. T., Koch R., 2007, ApJ, 654, 499
Kenyon S., Bromley B., 2017, ApJ, 844, 116

Kilic M., Redfield S., 2007, ApJ, 660, 641
Kilic M., Thorstensen J. R., Koester D., 2008, ApJ, 689, L45
Kissin Y., Thompson C., 2015, ApJ, 809, 108
Kochukhov O., Makaganiuk V., Piskunov N., 2010, A&A, 524, A5
Koester D., Provencal J., Shipman H. L., 1997, A&A, 230, L57
Koester D., Dreizler S., Weidemann V., Allard N. F., 1998, A&A, 338, 612
Koester D., Rollenhagen K., Napiwotzki R., Voss B., Christlieb N., Homeier D., Reimers D., 2005, A&A, 432, 1025
Koester D., Voss B., Napiwotzki R., Christlieb N., Homeier D., Lisker T., Reimers D., Heber U., 2009, A&A, 505, 441
Koester D., Gänsicke B. T., Farihi J., 2014, A&A, 566, A34
Kraft R. P., Burrows D. N., Nousek J. A., 1991, ApJ, 374, 344
Landstreet J. D., Borra E. F., Angel J. R. P., Illing R. M. E., 1975, ApJ, 201, 624
Landstreet J. D., Bagnulo S., Valyavin G. G., Fossati L., Jordan S., Monin D., Wade G. A., 2012, A&A, 545, A30
Landstreet J. D., Bagnulo S., Fossati L., 2012, A&A, 572, A113
Linsky J. L. et al., 2006, ApJ, 647, 1106
Lodders K., 2003, ApJ, 591, 1220
MacGregor M. A. et al., 2017, ApJ, 842, 8
Manser C. J. et al., 2016, MNRAS, 455, 4467
McCook G. P., Sion E. M., 1999, ApJS, 121, 1
McDonough W. F., 2000, in Teisseyre R., Majewski E., eds, Earthquake Thermodynamics and Phase Transformation in the Earth's Interior. Academic Press, San Diego, p. 5
Meng H. Y. A. et al., 2014, Science, 345, 1032
Metzger B. D., Rafikov R. R., Bochkarev K. V., 2012, MNRAS, 423, 505
Mukai K., 2017, PASP, 129, 062001
Nordhaus J., Wellons S., Spiegel D. S., Metzger B. D., Blackman E. G., 2011, PNAS, 108, 3135
Oliveira C. M., Moos H. W., Chayer P., Kruk J. W., 2006, ApJ, 642, 283
Pontoppidan K. M., Salyk C., Bergin E. A., Brittain S., Marty B., Mousis O., Öberg K. I., 2014, in Beuther H., Klessen R. S., Dullemond C. P., Henning T., eds, Protostars and Planets VI. Univ. Arizona Press, Tucson, p. 363
Rafikov R. R., 2011, ApJ, 732, L3
Rappaport S., Gary B. L., Kaye T., Vanderburg A., Croll B., Benni P., Foote J., 2016, MNRAS, 458, 3904
Redfield S., Farihi J., Cauley W. P., Parsons S. G., Gänsicke B. T., Duvvuri G. M., 2017, ApJ, 839, 42
Rocchetto M., Farihi J., Gänsicke B. T., Bergfors C., 2015, MNRAS, 449, 574
Schmidt G. D., Smith P. S., 1995, ApJ, 448, 305
Schmidt G. D. et al., 2003, ApJ, 595, 1101
Schure K. M., Kosenko D., Kaastra J. S., Keppens R., Vink J., 2009, A&A, 508, 751
Shulyak D., Tsymbal V., Ryabchikova T., Stütz Ch., Weiss W. W., 2004, A&A, 428, 993
Subasavage J. P. et al., 2017, AJ, 154, 32
Tout C. A., Wickramasinghe D. T., Liebert J., Ferrario L., Pringle J. E., 2008, MNRAS, 387, 897
Vallerga J. V., Vedder P. W., Craig N., Welsh B. Y., 1993, ApJ, 411, 729
van der Marel N., van Dishoeck E. F., Bruderer S., Andrews S. M., Pontoppidan K. M., Herczeg G. J., van Kempen T., 2016, A&A, 585, A58
Vanderburg A. et al., 2015, Nature, 526, 546
Vennes S., Kawka A., Németh P., 2010, MNRAS, 404, L40
Veras D., 2016, R. Soc. Open Sci., 3, 150571
Veras D., Carter P. J., Leinhardt Z. M., Gänsicke B. T., 2016, MNRAS, 465, 1008
Veras D., Marsh T. R., Gänsicke B. T., 2016, MNRAS, 461, 1413
Wilms J., Allen A., McCray R., 2000, ApJ, 542, 914
Wilson D. J., Gänsicke B. T., Koester D., Raddi R., Breedt E., Southworth J., Parsons S. G., 2014, MNRAS, 445, 1878
Wilson D. J., Gänsicke B. T., Farihi J., Koester D., 2016, MNRAS, 459, 3282

Wyatt M. C., Farihi J., Pringle J. E., Bonsor A., 2014, MNRAS, 439, 3371
Xu S., Jura M., 2014, ApJ, 745, 88
Xu S., Jura M., 2014, ApJ, 792, L39
Xu S., Jura M., Koester D., Klein B., Zuckerman B., 2014, ApJ, 783, 79
Xu S., Jura M., Dufour P., Zuckerman B., 2016, ApJ, 816, L22
Zuckerman B., Becklin E. E., 1987, Nature, 330, 138

Zuckerman B., Koester D., Reid I. N., Hünsch M., 2003, ApJ, 596, 477
Zuckerman B., Koester D., Melis C., Hansen B. M. S., Jura M., 2007, ApJ, 671, 872

This paper has been typeset from a TEX/LATEX file prepared by the author.